Available online at www.sciencedirect.com
ScienceDirect
Trans. Nonferrous Met. Soc. China 32(2022) 1691−1704

Transactions of
Nonferrous Metals
Society of China
www.tnmsc.cn

Recycling of waste carbon residue from spent lithium-ion batteries via constant-pressure acid leaching

Xiang-dong ZHU[1], Jin XIAO[1,2], Qiu-yun MAO[3], Zhen-hua ZHANG[1], Lei TANG[1], Qi-fan ZHONG[1,2]

1. School of Metallurgy and Environment, Central South University, Changsha 410083, China;
2. National Engineering Laboratory for Efficient Utilization of Refractory Nonferrous Metal Resources,
Central South University, Changsha 410083, China;
3. Department of Educational Science, Hunan First Normal University, Changsha 410205, China

Received 31 March 2021; accepted 20 October 2021

Abstract: Waste carbon residue (WCR) was efficiently detoxicated and regenerated to high-purity graphite (PGC) used in lithium-ion batteries through the constant-pressure acid leaching technique. The leaching conditions were optimized by the combination of orthogonal and single-factor experiments. Results show that PGC with 99.5% purity is regenerated at temperature of 60 °C, initial acid concentration of 12%, leaching time of 180 min, and liquid-to-solid ratio of 25:1, satisfying the requirements of commercial graphite. Meanwhile, the sodium hydroxide precipitation process was designed to recover valuable components from leachate efficiently. Ni, Co, Mn, and Al recoveries reach 96.92%, 87.5%, 97.83%, and 92.17%, respectively, at pH=11. Moreover, the co-product NaF can be recovered with purity over 99% via evaporative crystallization. The loss rate of fluorine is less than 0.5%, thereby eliminating the pollution risk of fluorine to the environment. The proposed process shows considerable environmental and economic benefits.

Key words: constant-pressure acid leaching; waste carbon residue; anode material regeneration; sodium hydroxide precipitation; NaF

---

1 Introduction

Recently, new energy vehicles have rapidly developed with the scale-up support of the national policy, promoting the rapid growth of the lithium-ion batteries (LIBs) industry [1,2]. During the long-term charging and discharging of LIBs, self-discharge, electrolyte decomposition, and the deterioration of electrode stability will inevitably occur, causing the batteries' capacity to decline rapidly and preventing their common use. LIBs will eventually be scrapped after 5−8 years [3]. The global LIBs recycling market reached 111783 t in 2018; the scrap amount is expected to reach approximately 641595 t in 2025, and less than 5% of them would have been recycled [4−6].

Currently, the recycling technology for spent LIBs mainly has been focused on hydrometallurgy for extracting valuable metal elements, such as lithium, nickel, cobalt, and manganese, from the mixture of cathode and anode materials [7−11]. Acid leaching and filtering produce the leaching residue called waste carbon residue (WCR), which contains graphite and valuable metals. No effective technical solution for harmlessness and resource utilization is available due to the complex composition of the WCR [12]. The WCR can only be disposed by stacking waste or high-temperature incineration, which leads to the massive waste of resources and severe environmental pollution [13,14].

Corresponding author: Qi-fan ZHONG, Tel: +86-18684965136, E-mail: 348259246@qq.com, zhongqifanchina@csu.edu.cn
DOI: 10.1016/S1003-6326(22)65903-X

Traditionally, chemical purification and physical purification are the main methods of graphite purification. The physical methods include flotation and high-temperature methods. The flotation method, which is an effective method of graphite purification, has the advantages of low cost and low environmental pollution [15]. Flotation can increase the concentrate of graphite to 80%–95%, but obtaining graphite with a purity above 99% is difficult [16]. The high-temperature method is used to obtain graphite carbon with a carbon content over 99.99% [17]. However, the thermal process for natural graphite to obtain a highly purified sample is costly, with amounts of carbon consumed via a high-temperature oxidation reaction.

The chemical purification includes alkali-acid [18,19], chlorination roasting [20], and hydrofluoric acid [21]. Among them, the hydrofluoric acid method is the most effective purification method due to its advantage of simple production process, high product purity, and no damage to the structure of graphite. However, hydrofluoric acid is corrosive and requires relatively high-end equipment, especially under high-temperature and high-pressure conditions. Meanwhile, the WCR is difficult to purify because its composition is more complex than natural graphite. Thus, this research explores the maximum purification efficiency with the minor hydrofluoric acid under constant temperature and pressure conditions.

This work aims to explore the optimal detoxification of the WCR to demonstrate the feasibility of regeneration and reuse. Constant-pressure acid leaching, selective precipitation, evaporation, and crystallization are coupled and matched innovatively after analyzing the element composition, microstructure, and phase composition of the WCR through ICP-OES, scanning electron microscopy–energy dispersive spectrometry (SEM−EDS), and XPS. Meanwhile, various physical properties of high-purity graphite (PGC) are analyzed to prove the possibility of regeneration. In addition, the comprehensive treatment of fluorine-containing leachate is processed to achieve efficient recovery of valuable metals and NaF products. Finally, an economic benefit analysis is performed to evaluate the industrial application potential of the proposed detoxification treatment.

2 Experimental

2.1 Material preparation

A resource recycling company provided the spent LIB materials used here. After disassembly, crushing, and mechanical sieving, the mixed powder of cathode and anode materials was leached with sulfuric acid to extract valuable metals, such as nickel, cobalt, manganese, and lithium. The leaching residue was obtained by filtering, that was, the WCR sample. Then, the sample was completely dissolved in aqua regia ($HCl:HNO_3=3:1$, volume ratio) to determine the chemical composition through ICP-OES. The carbon content was tested using the graphite chemical analysis method. The chemical composition of the WCR is given in Table 1.

Table 1 Chemical composition of WCR (wt.%)

Li	Ni	Co	Mn	C	F	P
0.09	1.22	0.28	0.41	94.77	1.03	0.14
Al	**S**	**Na**	**Cu**	**Fe**	**Ca**	**Si**
0.21	0.68	0.25	0.08	0.19	0.02	0.56

2.2 Experiment and procedures

The main steps of this experiment were as follows:

(1) Raw material preparation: A 20 g sample was dried for 10 h at 110 °C and ground.

(2) Hydrofluoric acid leaching: A specific concentration of the HF solution was configured, and the raw material was stirred and leached under the set liquid-to-solid (L/S) ratio to control the leaching time and temperature.

(3) Filtering: The leaching residue was washed several times, and the pH value was constantly checked until the pH was near seven; then, the residue was dried in a vacuum drying oven at 110 °C for 10 h.

(4) Result analysis: The carbon content was determined by decarburization at 900 °C for 4 h.

(5) Precipitation and filtering: The pH of leaching solutions was adjusted by adding sodium hydroxide until it reached 11. After filtration, the precipitated product of the nickel−cobalt−manganese hydroxide precipitation was obtained.

(6) Evaporative crystallization: Evaporative

crystallization was used to crystallize the NaF products.

The flow diagram for the HF leaching process is illustrated in Fig. 1.

2.3 Characterization

The phase and the crystalline structure were analyzed by X-ray diffraction (XRD, Empyrean 2) via Cu K_α radiation in the 2θ range of 10°−90° at a scanning rate of 2 (°)/min. The element of the sample was analyzed through ICP-OES (CAP7400Radial). The morphology of the samples was characterized by field-emission scanning electron microscopy (FESEM, JSM-7900F) and energy dispersive spectroscopy (EDS, EDAX Octane X). The particle size distribution of the sample was tested with a laser particle size analyzer (Mastersizer 2000). The surface feature of the elemental electron states was studied via XPS (Escalab Xi+) with Al K_α X-ray radiation. The internal surface area of the supported catalysts was measured using the BET method with a surface area analyzer (Micromeritics 2460). Thermal gravimetric analysis was performed using thermogravimetry−differential thermal equipment (SDT 650).

3 Results and discussion

3.1 Material investigation

Table 1 shows the low content of impurity elements with complicated components. If these elements were directly recycled into the graphite anode of LIBs, then they will inevitably cause the metal impurities to react with the electrolyte to generate fluoride salts, causing particular problems, such as reducing the first-cycle coulomb efficiency and excessive electrolyte consumption. Moreover, the metal ions will form a microcircuit, causing the battery to physically self-discharge and reduce the voltage. First, the WCR must be purified to over 99.5%. SEM−EDS was used to characterize the sample's morphology and the element's distribution to achieve this goal. The results are shown in Figs. 2 and 3.

The WCR maintains a graphite-layered crystal structure (Fig. 2). Meanwhile, the graphite in the WCR is mainly spherical with a particle size of 5−10 μm and has an apparent layered flake structure, which is consistent with characteristics of natural flake graphite [22]. Figure 3 shows the distributions of the element from EDS. The coincidence degree between Si and O is relatively high, presumably because the possible compound is SiO_2. Element Al may combine with F and generate AlF_3.

To gain further information on the structure and composition, XPS was used to investigate the electronic state of the elements in the near-surface region. The corresponding results are presented in Fig. 4. The WCR is fitted using three contributions centered around 284, 286.0, and 290.3 eV (Fig. 4(a)). These phenomena can be attributed to the sp^2 and sp^3 hybridized carbon structures of C—C and C═C in the binding energy (BE) of 284.8 eV. However, 286.0 and 290.3 eV are also assigned to the sp^3 hybridized carbon structures of C—C—O, O—C═O, and C═O [23].

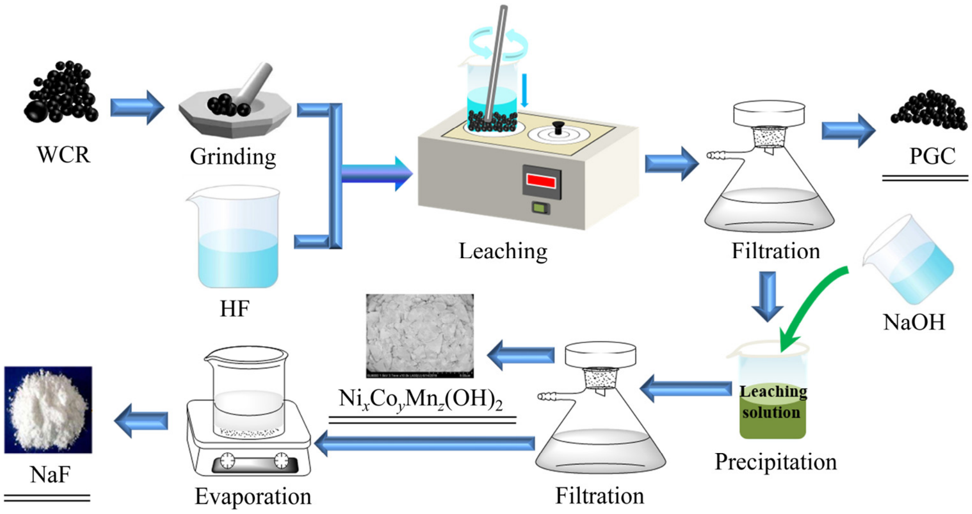

Fig. 1 Flow diagram for HF leaching process

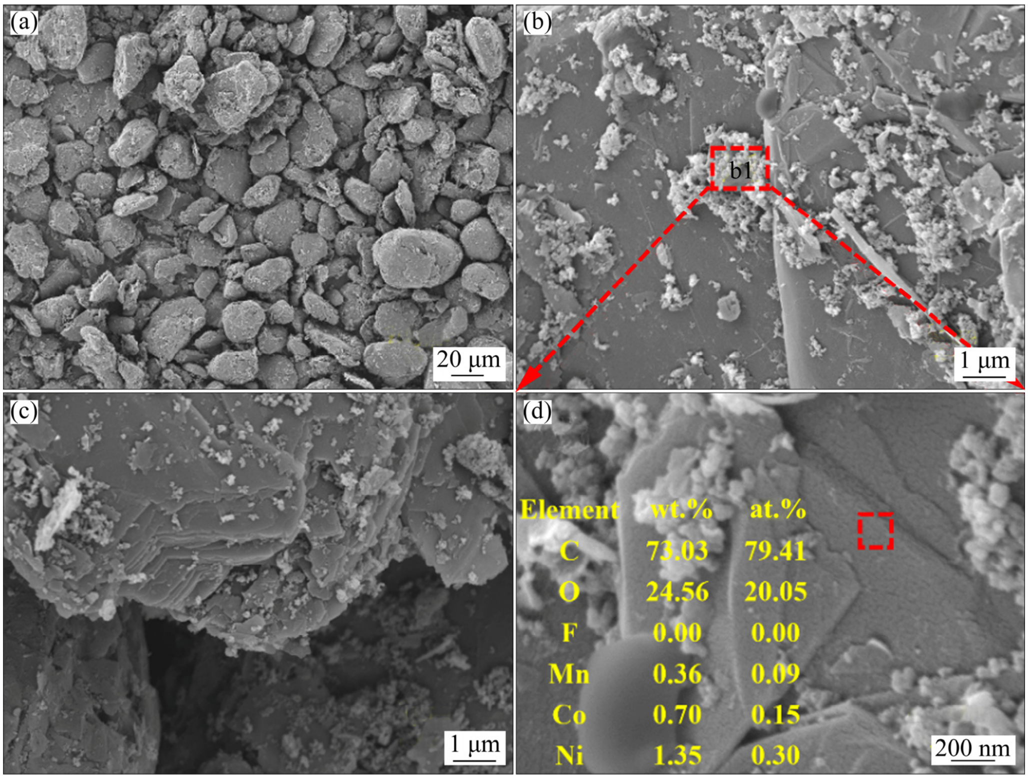

Element	wt.%	at.%
C	73.03	79.41
O	24.56	20.05
F	0.00	0.00
Mn	0.36	0.09
Co	0.70	0.15
Ni	1.35	0.30

Fig. 2 SEM images of WCR (a, b, c) and partial enlarged SEM image of b1 area (d)

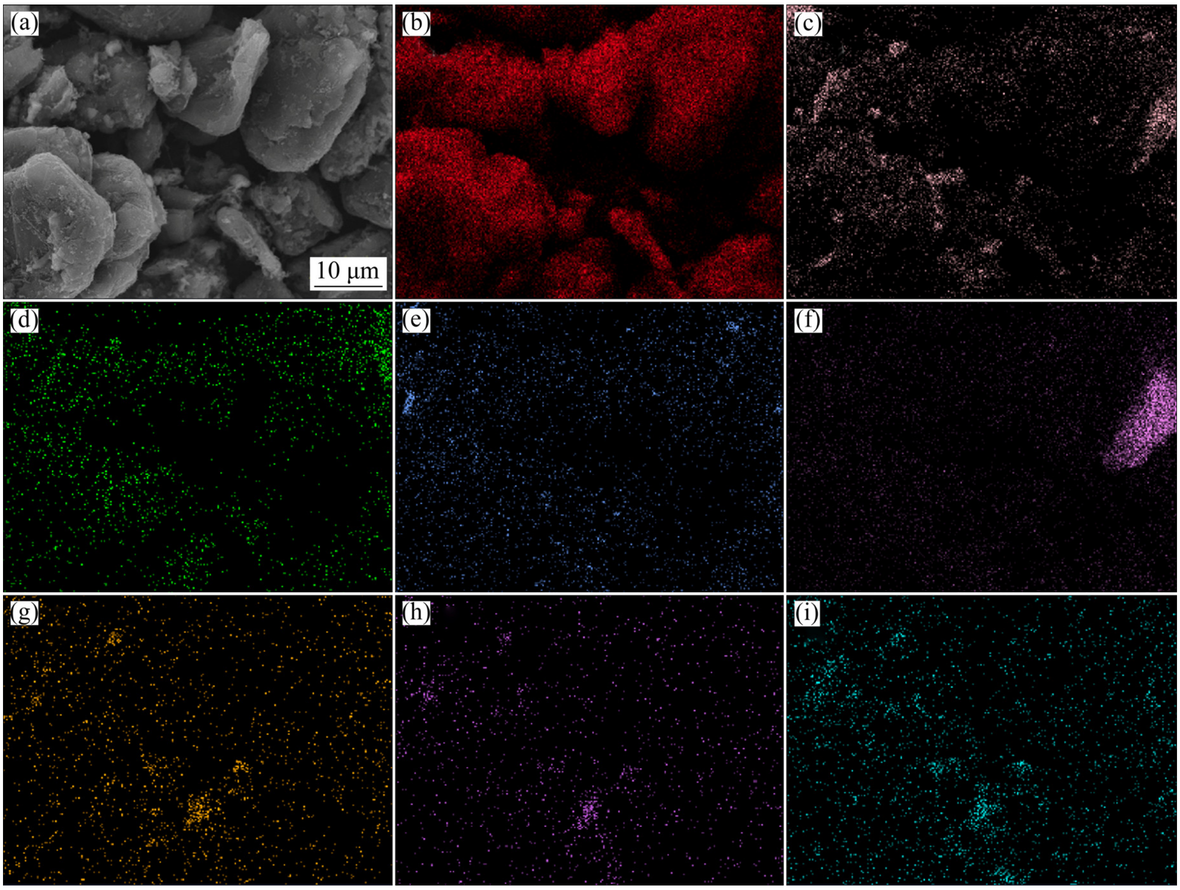

Fig. 3 SEM image (a) and EDS elemental distributions of WCR: (b) C; (c) O; (d) F; (e) Al; (f) Si; (g) Mn; (h) Co; (i) Ni

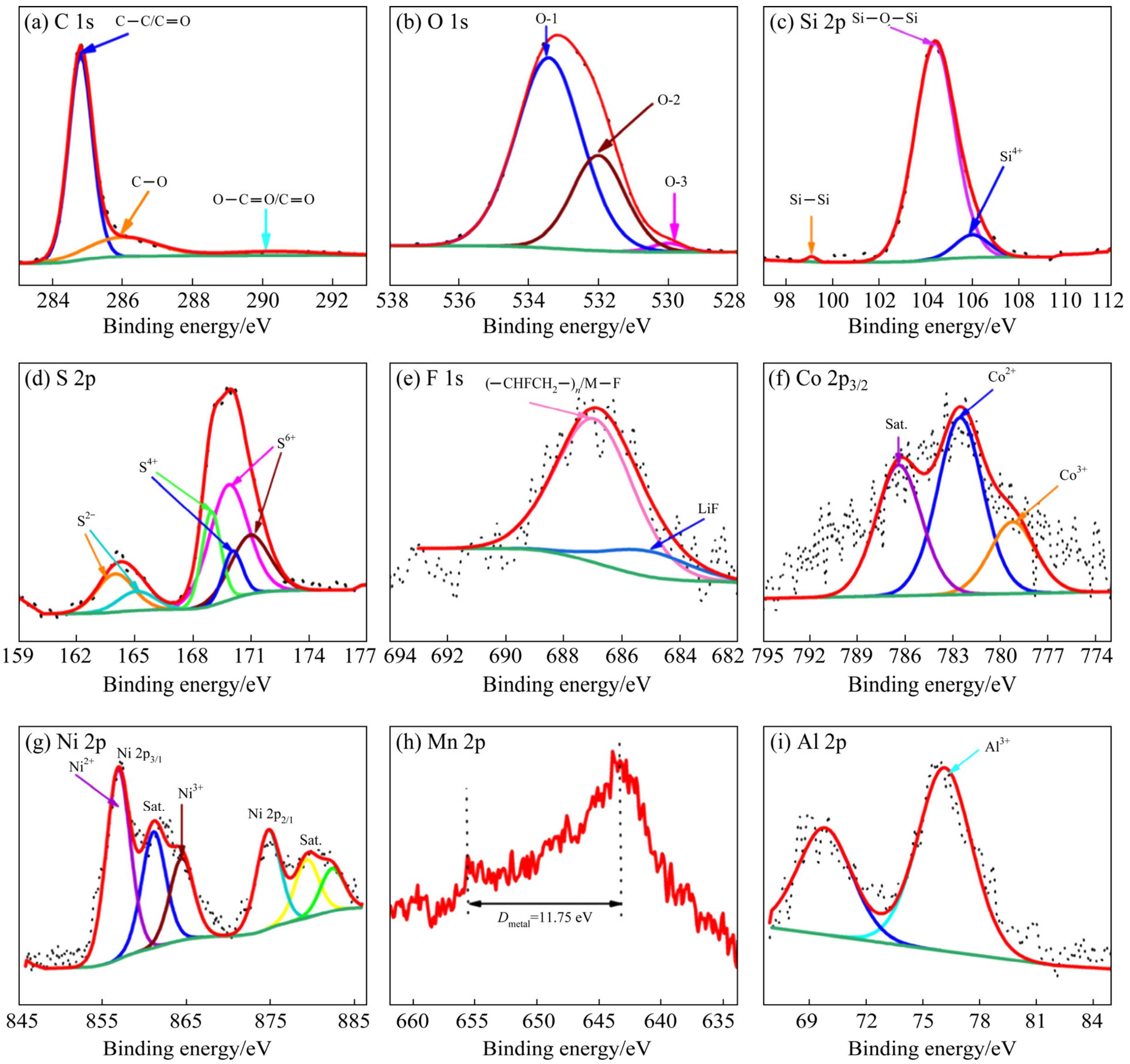

Fig. 4 XPS spectra of WCR: (a) C 1s; (b) O 1s; (c) Si 2p; (d) S 2p; (e) F 1s; (f) Co $2p_{3/2}$; (g) Ni 2p; (h) Mn 2p; (i) Al 2p

The result also shows that the WCR has a prominent sp^2 bonding component. In Fig. 4(b), O 1s can be fitted with three distinct peaks, namely, the organic oxygen at 533.5 eV (O-1), the hydrated or defective oxide at 531.5 eV (O-2), and the lattice oxide of C—O at 530.0 eV (O-3) [24].

Three distinct peaks are illustrated in Fig. 4(c). The low energy peak (99.10 eV) corresponds to the Si—Si bonding in pure Si. The BE of the high-intensity peaks is 104.39 eV, which agrees with that of SiO_2 [25]. At approximately 106 eV of the BE, Si is assigned to Si^{4+}. In combination with the XPS in Figs. 4(b, e), the possible compounds are SiO_3^{2-} or SiF_6^{2-} [26,27].

The valence state of the sulfur species and the chemical environment of various elements in the WCR are shown in Fig. 4(d). The other peak at 163.99 eV is typically attributed to the sulfur–metal bonds [28]. The peaks at 169.84 and 170.94 eV are attributed to the $2p_{3/2}$ and $2p_{1/2}$ of S^{6+}, respectively. The peaks at 168.94 and 170.04 eV are attributed to the $2p_{3/2}$ and $2p_{1/2}$ of S^{4+}, respectively [29]. The BE of sulfur over 168.4 eV was generally attributed to sulfate [30]. Therefore, the S in the raw material exists in the form of S^{2-}, SO_3^{2-}, and SO_4^{2-}.

The XPS of F in Fig. 4(e) fits two distinct peaks with BEs of 685.1 and 686.94 eV. The BE of 685.1 eV corresponds to LiF [31]. According to BEAMSON and BRIGGS [32], the BE of 686.94 eV corresponds to $(-CHFCH_2-)_n$, consistent with our simulation. According to the source of the sample, the BE is further speculated to be a PVDF binder. However, the BE of 686.94 eV matches that of Na_2SiF_6. In combination with Fig. 4(j), the XPS analysis of Al shows that the BE of Al_2O_3 is approximately 74.7 eV. The addition of F^- increases the BE of Al. When the BEs of Al and F are 76.16 and 686.94 eV, respectively, they can be determined as AlF_3 or AlF_6^{3-} [33].

Figure 4(f) shows that the Co $2p_{3/2}$ is fitted with two peaks, namely, 779.23 and 782.52 eV, which are the characteristic peaks of Co^{3+} and Co^{2+}, respectively. Thus, Co exists in two valence states: Co^{3+} and Co^{2+} [34].

The Ni 2p spectra (Fig. 4(g)) are best fitted with two spin-orbit doublets, which are the characteristics of Ni^{2+} and Ni^{3+} and two shake-up satellites (indicated as “Sat.”). The peaks of the Ni $2p_{3/2}$ and Ni $2p_{1/2}$ spectra located at 856.90 and 874.77 eV with satellite peaks at 864.46 and 882.36 eV are assigned to Ni^{2+} and Ni^{3+}, respectively [35,36].

The concentration of Mn ions in the surface and near-surface layers is low. Consequently, curve-fitting analysis cannot be performed accurately on the Mn 2p spectra. Nevertheless, two peaks appear in the XPS spectrum (Fig. 4(h)) because of Mn $2p_{3/2}$ and Mn $2p_{1/2}$ for Mn, with a spin-energy separation of 11.75 eV. It is suggested that the Mn cations in these oxides possess an average valence near four [37]. This work speculates that the sample may be in MnO_2 or MnS_2 form.

In combination with the results of the ICP-OES, SEM−EDS, and XPS analyses, the compounds in the WCR can be roughly estimated to be LiF, AlF_3, $CoSO_4$, Co_3S_4, $CoSO_3$, NiO, $NiSO_4$, Ni_3S_4, MnO_2, MnS_2, SiO_2, Na_2SiF_6, Na_2SiO_3, Na_3AlF_6, and PVDF.

3.2 Constant-pressure hydrofluoric acid leaching

3.2.1 Thermodynamic calculation

The relationships between the $\Delta G^{\ominus}$ and the temperature for the possible reactions of fluoride, oxide, and sulfide during hydrofluoric acid leaching are shown in Fig. 5. Figure 5(a) indicates that the reaction product of MnO_2 and HF could only generate O_2 but not F_2. Meanwhile, MnO_2 is transformed into acid-soluble MnF_2 or MnF_3. This phenomenon indicates that the oxides in the WCR could react with HF and be converted to acid-soluble fluoride salts. Fluoride salts, such as AlF_3 and LiF, can be further transformed into acid-soluble complex salts. Figure 5(b) indicates that sulfate reactions occur in the solution; thus, the species are in the state of ions, such as Co^{2+}, Co^{3+}, Ni^{2+}, and Mn^{2+}. The result of the thermodynamic calculations indicates that metal ions react with HF to generate the corresponding acid-soluble fluorides. Given that the produced cobalt trifluoride is unstable, it will react with water to form cobalt difluoride. Meanwhile, the sulfite could react with HF to produce fluoride and SO_2. The metal sulfide could also react with HF to form fluoride, hydrogen sulfide, or sulfur under constant pressure. Therefore, hydrofluoric acid leaching and the impurity process could thermodynamically convert insoluble fluoride, oxide, and metal sulfides to soluble fluoride and complete a phase transformation.

3.2.2 Orthogonal experiments

In the hydrofluoric acid leaching and purification experiment, many factors affect the carbon content of the PGC, such as temperature, time, L/S ratio, and initial acid concentration. This work conducted a 4-factor and 3-level ($L_9(3^4)$)

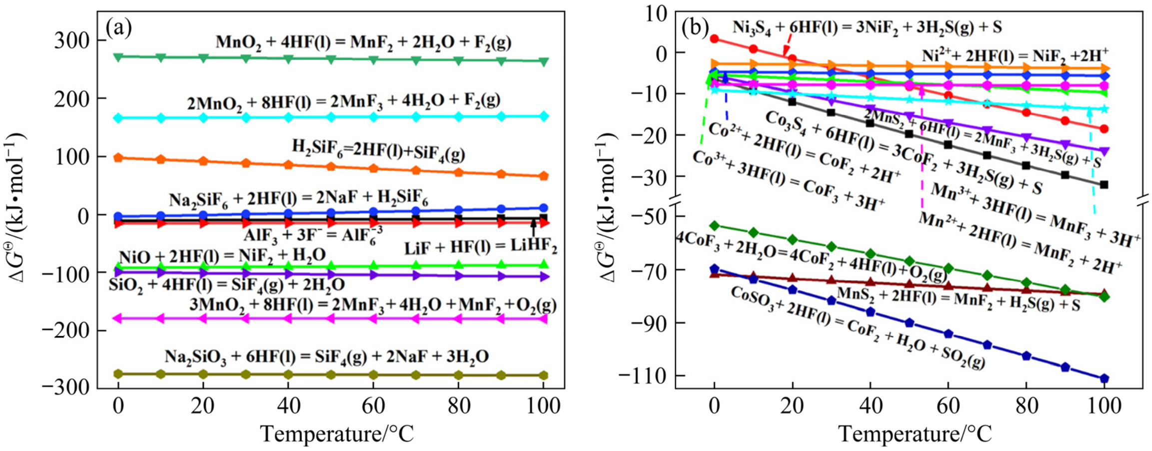

Fig. 5 Relationship between $\Delta G^{\ominus}$ and temperature for possible reactions of fluoride or oxide (a) and sulfide (b)

orthogonal experiment to explore the primary and secondary factors affecting the results herein; the extreme values of the final result were used to determine the primary and secondary relationships among different experimental factors. The results are given in Tables 2 and 3.

Table 2 Orthogonal design table of acid leaching

Level	Factor			
	Temperature (A)/°C	Time (B)/min	L/S ratio (C)/ (mL·g^{-1})	Initial acid concentration (D)/%
1	30	60	5:1	2
2	50	120	15:1	12
3	70	180	25:1	22

Table 3 Results of orthogonal experiments

Test No.	Factor				Carbon content/%
	A	B	C	D	
1	1 (30)	1 (60)	1 (5:1)	1 (2)	98.06
2	1 (30)	2 (120)	2 (15:1)	2 (12)	98.48
3	1 (30)	3 (180)	3 (25:1)	3 (22)	99.00
4	2 (50)	1 (60)	2 (15:1)	3 (22)	99.18
5	2 (50)	2 (120)	3 (25:1)	1 (2)	98.78
6	2 (50)	3 (180)	1 (5:1)	2 (12)	99.34
7	3 (70)	1 (60)	3 (25:1)	2 (12)	99.47
8	3 (70)	2 (120)	1 (5:1)	3 (22)	99.52
9	3 (70)	3 (180)	2 (15:1)	1 (20)	99.32
$K1$	295.54	296.71	296.92	296.16	
$K2$	297.3	296.78	296.98	297.29	
$K3$	298.31	297.66	297.25	297.7	
$k1$	98.51	98.90	98.97	98.72	
$k2$	99.1	98.93	98.99	99.10	
$k3$	99.44	99.22	99.08	99.23	
R	0.93	0.32	0.11	0.51	

Table 3 shows that the primary and secondary factors affecting the purification effect of hydrofluoric leaching follow the order of temperature > initial acid concentration > time > L/S ratio. The range of the leaching temperature is the largest, and that of the L/S ratio is the smallest. The orthogonal experiments also demonstrate that the best combination of the main factors in the hydrofluoric acid leaching purification process is $A_3B_3C_3D_3$. Specifically, the best leaching temperature, leaching time, leaching L/S ratio, and initial hydrofluoric acid concentration are 70 °C, 180 min, 25:1, and 22%, respectively.

3.2.3 Single-factor experiments

To maximally reduce the impurity content of the final product, single-factor experiments were carried out to explore the conversion behavior of hydrofluoric acid leaching and optimize the parameters. The effects of various parameters on the hydrofluoric acid leaching efficiency are shown in Fig. 6.

(1) Effect of leaching temperature on carbon content

Figure 6(a) shows that the carbon content increases from 99% to 99.56% under constant pressure when the leaching temperature increases from 30 to 70 °C. The increase in temperature is conducive to the leaching of impurity elements. However, the increase in temperature has little effect on the leaching of impurities (decreasing trend) when the temperature exceeds 60 °C. This could be attributed to the noncarbon impurity elements in the WCR that combine with F to form fluoride or complex salts during HF leaching. The thermodynamic calculation shown in Fig. 5 indicates that equilibrium constant K shows a decreasing trend with increasing the temperature in some reactions. This result indicates that the reverse reaction trend increases with the temperature, which is conducive to the removal of noncarbon impurity elements.

From a kinetics perspective, the increase in temperature is conducive to the mobility of ions in the aqueous solution, enhancing the kinetic energy and disordered operation of the ions participating in the reaction in the solution. This also reduces the energy barrier of the chemical reaction and increases the number of activated molecules per unit volume of the reactant. Moreover, the probability of effective collision reaction increases, the reaction becomes intenser and smoother, and the reaction rate increases. However, the HF volatilization speed increases with the temperature, thus reducing the concentration of hydrofluoric acid in the solution and affecting the leaching efficiency of impurities. Therefore, the considered leaching temperature is 60 °C.

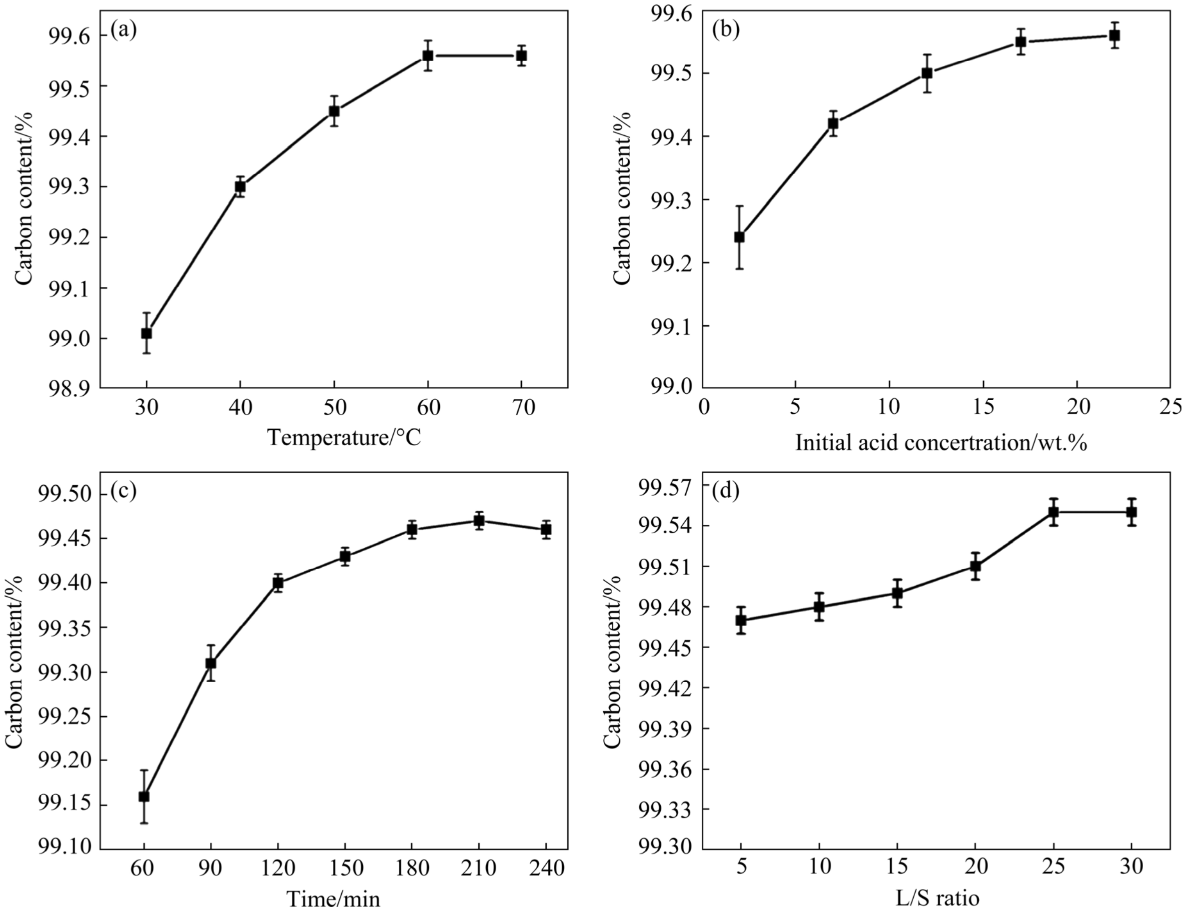

Fig. 6 Effects of temperature (a), initial acid concentration (b), time (c), and L/S ratio (d) on carbon content of PGC

(2) Effect of initial acid concentration on carbon content

Figure 6(b) shows that the carbon content of the PGC is 99.24% when the initial acid concentration is 2%. The carbon content of the PGC gradually increases with the initial acid concentration. Specifically, the leaching rate of impurities gradually increases. When the concentration increases to 12%, the carbon content of the PGC reaches 99.5%, satisfying the requirements of graphite anode materials. The continuous increase of the concentration has little effect on the carbon content. However, the carbon content of the PGC tends to balance when the concentration exceeds 12%. This phenomenon occurs because the amount of hydrofluoric acid is insufficient to react under the low acid concentration. The generated NiF_2, CoF_2, and other fluoride salts are soluble in acid and insoluble in water. Under low-concentration acidic conditions, the solubility decreases. The generated fluoride salt is adhered to the graphite surface, decreasing the removal efficiency of impurities in the WCR. However, the noncarbon impurity elements are fully reacted when the initial acid concentration reaches 12%. Therefore, the continued increase of the initial acid concentration has little effect on the carbon content of the PGC when the initial acid concentration reaches 12%. Meanwhile, the corrosivity and cost increase with the concentration of the hydrofluoric acid. Therefore, the initial acid concentration is set to be 12% after careful consideration.

(3) Effect of leaching time on carbon content

Figure 6(c) shows that the carbon content of the PGC first increases with the prolonging of the leaching time, then levels off, and finally decreases slightly. When the leaching time is less than 180 min, the reaction in the system is incomplete. The chemical reactions in the HF leaching system reach the balance in 180 min. The continued increase of the leaching time may cause the volatilization of the hydrofluoric acid in the solution. Therefore, the optimal leaching time selected is 180 min after comprehensive consideration.

(4) Effect of L/S ratio on carbon content

Figure 6(d) shows that increasing the L/S ratio can promote the separation of noncarbon impurity elements and graphite. When the L/S ratio is 25:1, the carbon content of the PGC reaches the maximum value, 99.54%. This phenomenon occurs because the L/S ratio is also an essential factor in the leaching kinetics. If the L/S ratio is low, then the viscosity of the solution increases, hindering the diffusion of solutes into the solution. The soluble fluoride salt solution can be saturated and crystallized in a low L/S ratio. If the crystal is wrapped around the reaction nucleus, then the contact between the unreacted nucleus and the solution is hindered and the leaching reaction rate is reduced. Therefore, the optimal L/S ratio is set to be 25:1 after comprehensive consideration.

3.3 Characterization of PGC

Figure 7 presents a comparison of the phase composition, crystal structure, and surface morphology of the WCR and the PGC treated under optimal conditions.

After purification, the amounts of impurity elements on the surface of the graphite significantly decrease. This result is consistent with the XRD pattern in Figs. 7(c, d). The result indicates that the impurities, such as nickel, cobalt, and manganese, are removed after treatment by constant-pressure hydrofluoric acid leaching. The main impurity elements of the final purified carbon product are aluminum compounds because the AlF_3 generated is insoluble in acid. The purity can exceed 99.5% and reaches the graphite anode standard of LIBs.

Figure 7(a) shows that the (002) diffraction peaks of the PGC are strengthened, demonstrating the improvement of the crystallinity and purity of the PGC. After the treatment, the interlayer spacing of the PGC increases and reaches d_{002}=0.3361 nm. This phenomenon is caused by forming a graphite intercalation compound due to the significant gaps between the carbon atom layers of graphite. High-affinity halide (fluoride) and acid can be easily inserted, expanding the carbon layer spacing [38]. The Mering–Marie formula could be used to calculate the graphitization degree of the PGC:

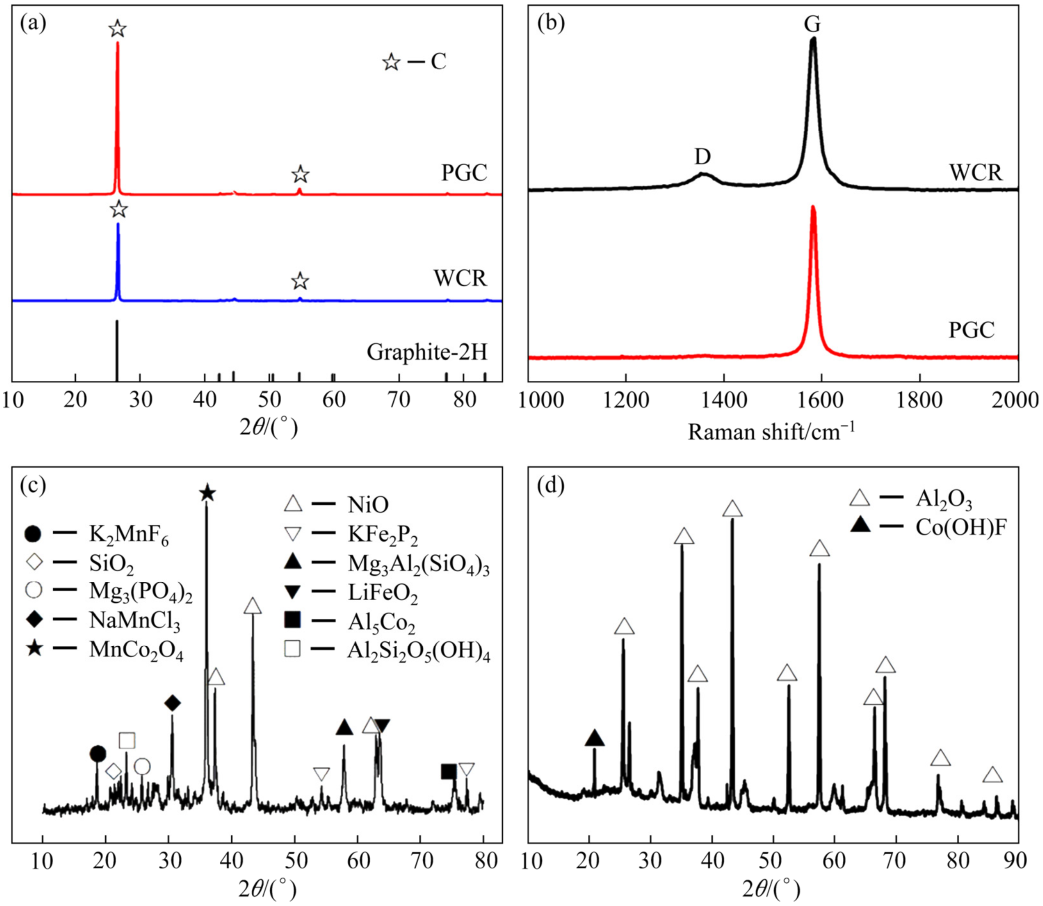

Fig. 7 Characterization of WCR and PGC treated under optimal conditions: (a) Comparison in XRD pattern; (b) Comparison in Raman spectra; (c) XRD pattern of ash content for WCR; (d) XRD pattern of ash content for PGC

$$G=[(0.344-d_{002})/0.3440-0.3354]\times 100\% \quad (1)$$

The graphitization degree of PGC (91.86%) is obtained through calculation. This result is consistent with the Raman spectrum analysis in Fig. 7(b) and indicates that the graphitization degree of the PGC significantly is improved after purification by hydrofluoric acid. Peak D in the Raman spectra nearly disappears. The results show that the PGC could also meet the graphite anode standard of LIBs for graphitization degree.

Figure 8(a) shows that the particle size of the PGC is mainly concentrated at 19.205 μm. Micromeritics 2460 was used to test the specific surface area at −195.85 °C. Before the test, the sample was vacuum degassed at 300 °C for 16 h, and the specific surface area of the PGC is 23.0930 m²/g. This phenomenon occurs because the WCR is mixed with a certain amount of conductive carbon black particles, such as Super-P or acetylene black, which increases the specific surface area of the PGC. However, carbon black is added as a conductive agent during the preparation of the graphite anode of LIBs. Therefore, adding different proportions of carbon black to compensate for this defect is challenging to control. Figure 8(b) shows that the mass loss rate of the WCR is significantly higher than that of the PGC. The graphite in the WCR begins to oxidize at approximately 510 °C. The oxidation reaction speed sharply increases with the temperature, and it is completed at 900 °C. After oxidation and combustion, the mass loss rate reaches 93.24%, while the graphite in the PGC only begins to oxidize at approximately 630 °C. The mass loss rates are only 17.1% and 23.62% at 900 °C and 1000 °C, respectively. These results are obtained because the valuable metal elements in the WCR act as catalysts during oxidation and combustion, thus accelerating the oxidation and combustion rates. This finding indicates that the PGC can obtain high purity and thermal stability after experimental purification.

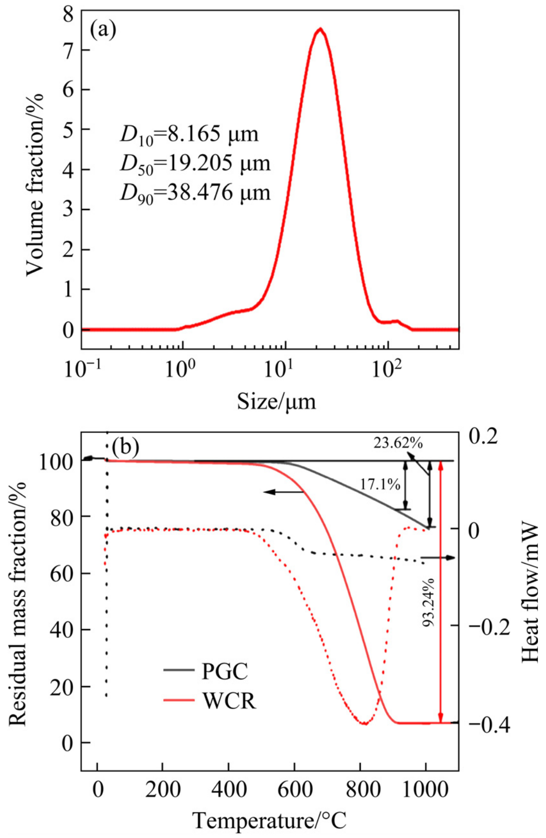

Fig. 8 Particle size of PGC (a); comparison in TG−DTG curves of WCR and PGC (b)

3.4 Recovery of valuable components

The leaching solution contains metal fluorides combined with HF, such as CoF_2, NiF_2, and MnF_2. To recover the valuable metal elements from the leaching solution, the potential−pH diagram of Ni−Co−Mn−H_2O in hydrofluoric acid leaching system at 25 °C is shown in Fig. 9. It is demonstrated that nickel, cobalt, and manganese ions are prone to precipitate with increasing pH in the fluoride salt system solution. The pH values of the precipitates of cobalt, nickel, and manganese are 6.41, 7.41, and 9.535, respectively. Therefore, the co-precipitation of nickel, cobalt, and manganese can be obtained by adjusting the pH of the solution.

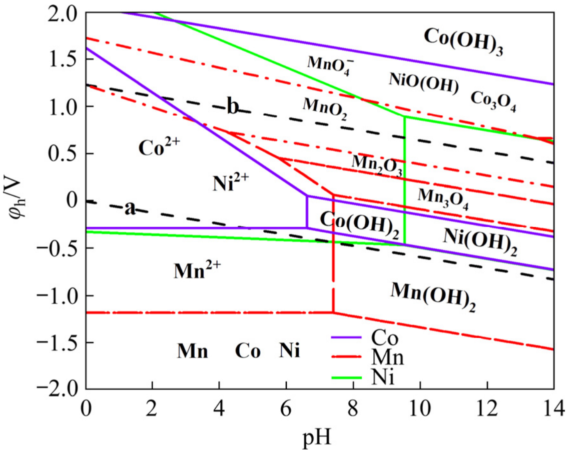

Fig. 9 Potential−pH diagram of Ni−Co−Mn−H_2O at 25 °C

First, NaOH was used for the adjustment. The pH reached 11 and enabled the valuable metal elements to produce water-insoluble hydroxide precipitates, such as $Ni_xCo_yMn_z(OH)_2$ and $Al(OH)_3$. The precipitation temperature was 25 °C, and the precipitation time was 6 h. The characterization of the sodium hydroxide precipitation residue is shown in Fig. 10.

Figure 10(a) shows that the sodium hydroxide precipitation residue has a good spherical morphology, and its surface can also adsorb some undissolved sodium salt crystals. Figure 10(b) indicates that the contents of Ni, Co, Mn, Al, and Si in the precipitate are 15.15%, 3.16%, 5.71%, 2.48%, and 8.96%, respectively. And the recovery rate of metal ions is calculated by the following formula:

$$L_i = \frac{C_i m_\text{p}}{C_{i0} m_0} \times 100\% \tag{1}$$

where L_i is the recovery rate of metal ions, m_p is the mass of the obtained precipitate (1.561 g), m_0 is the mass of the experimental sample (20 g), C_{i0} and C_i are the content of metal ions in the experimental sample and precipitate. Therefore, 96.92% Ni, 87.5% Co, 97.83% Mn, and 92.17% Al can be recycled under alkaline conditions with a pH of 11 according to Eq. (1). However, the recovery rate of silicon is more significant than 100% because the fluoride ions can corrode the glass, thereby increasing the silicon content.

After precipitation and recovery of valuable components such as nickel, cobalt, and manganese, the process of evaporative crystallization was used to crystallize the NaF products. And the characterization of the NaF products is shown in Figs. 11 and 12.

Figure 11(a) shows that NaF recovered via evaporative crystallization product has a pyramidal morphology. Meanwhile, the results of EDS mapping (Fig. 11(b)) and XRD pattern (Fig. 12) prove that the crystalline product is sodium fluoride with a purity exceeding 99%. Although hydrofluoric acid is used in this approach, more than 99.5% of fluorine is recovered in the form of NaF, thereby eliminating the pollution risk of

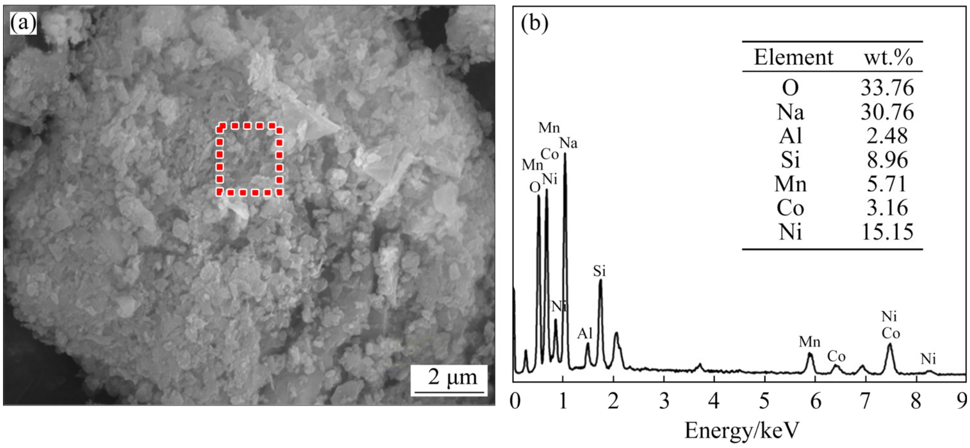

Element	wt.%
O	33.76
Na	30.76
Al	2.48
Si	8.96
Mn	5.71
Co	3.16
Ni	15.15

Fig. 10 Characterization of sodium hydroxide precipitation residue: (a) SEM image; (b) EDS mapping

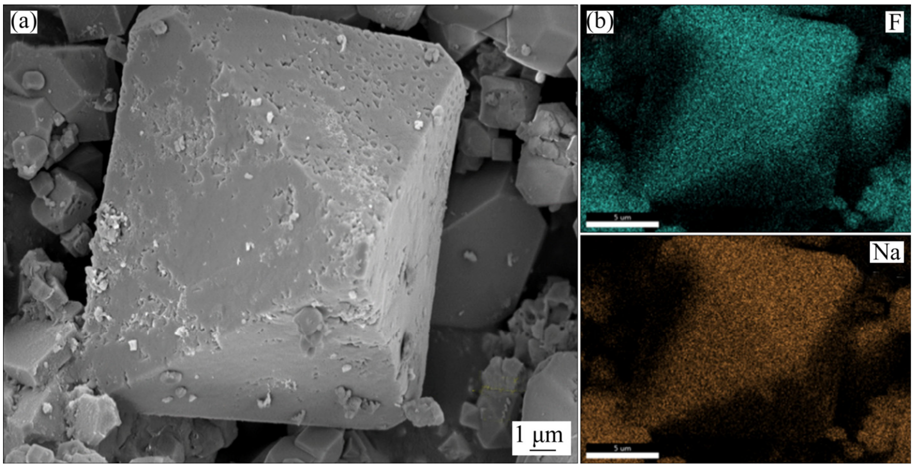

Fig. 11 Characterization of NaF product: (a) SEM image; (b) EDS mapping

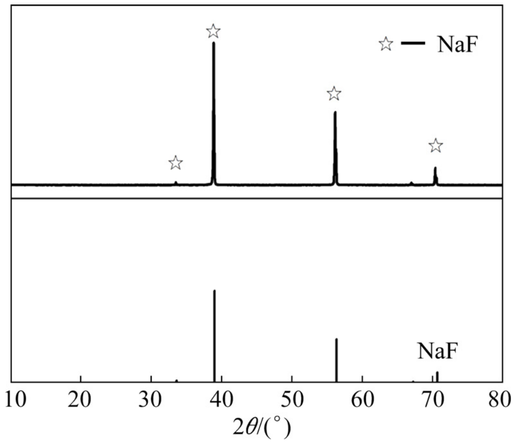

Fig. 12 XRD pattern for NaF product

fluorine to the environment. The proposed process could sequentially recycle the PGC, nickel−cobalt−manganese hydroxide precipitates, aluminum hydroxide, and NaF from the WCR. Moreover, nearly no effluent liquor, waste residue, and gas would be discharged during the proposed process, indicating substantial environmental benefits.

3.5 Economic benefit analysis

Economic benefit analysis was implemented to evaluate the large-scale application potential of the proposed WCR harmless treatment and regeneration of graphite. The results show that the economic benefit of the purification of 1 kg of WCR is RMB ￥2.466, whereas the burning cost of hazardous solid waste in China is usually RMB￥2.9−3.0. Meanwhile, an additional economic benefit of RMB￥28.54 could be obtained by the two HF cycles, which is proven to be feasible. Hence, the proposed process can realize the onsite harmless treatment and regeneration of graphite with remarkable environmental and economic benefits.

4 Conclusions

(1) Under optimized conditions (i.e., leaching temperature of 60 °C, initial acid concentration of 12%, leaching time of 180 min, and L/S of 25:1), the PGC with a purity of 99.5%, a graphitization degree of 91.86%, D_{50}=19.205 μm, and high thermal stability is recovered.

(2) Sodium hydroxide was used as a precipitating agent to recover Ni, Co, Mn, and Al from the leachate. Under specific precipitation conditions (i.e., pH =11, temperature of 25 °C, and precipitation time of 6 h), 96.92%, 87.5%, 97.83%, and 92.17% of Ni, Co, Mn, and Al can be recovered.

(3) More than 99.5% of fluorine is recovered in the form of NaF via evaporation crystallization, eliminating the pollution risk of fluorine to the environment. Moreover, nearly no effluent liquor, waste residue, and gas would be discharged during the proposed process.

(4) The economic benefit of the purification of 1 kg of WCR is RMB ￥ 2.466, and the economic benefit could be increased to more than RMB￥31/kg by the two HF cycles. Compared with burning, the proposed process provides additional income while eliminating environmental pollution risks, realizing graphite regeneration, and recovering valuable components.

Acknowledgments

The authors are grateful for the financial supports from the National Natural Science Foundation of China (Nos. 52174338, 51904349) and the Natural Science Foundation of Hunan Province, China (No.2021JJ30796).

References

[1] YANG Jian, JIANG Liang-xing, LIU Fang-yang, JIA Ming, LAI Yan-qing. Reductive acid leaching of valuable metals from spent lithium-ion batteries using hydrazine sulfate as reductant [J]. Transactions of Nonferrous Metals Society of China, 2020, 30: 2256−2264.

[2] FAN Xiao-ping, TAN Chun-lei, LI Yu, CHEN Zhi-qiang, LI Ya-hao, HUANG You-guo, PAN Qi-chang, ZHENG Feng-hua, WANG Hong-qiang, LI Qing-yu. A green, efficient, closed-loop direct regeneration technology for reconstructing of the $LiNi_{0.5}Co_{0.2}Mn_{0.3}O_2$ cathode material from spent lithium-ion batteries [J]. Journal of Hazardous Materials, 2020, 19: 124610.

[3] ZHANG Xiao-xiao, LI Li, ERSHA F, XUE Qing, BIAN Yi-fan, WU Feng, CHEN Ren-jie. Toward sustainable and systematic recycling of spent rechargeable batteries [J]. Chemical Society Reviews, 2018, 47: 7239−7302.

[4] WANG Jian-bo, LV Juan, ZHANG Ming-xing, TANG Mi-qi, LU Qi, QIN Yu-fei, LU Yan, YU Bo. Recycling lithium cobalt oxide from its spent batteries: An electrochemical approach combining extraction and synthesis [J]. Journal of Hazardous Materials, 2020, 405: 124211.

[5] REN Guo-xing, XIAO Song-wen, XIE Mei-qiu, PAN Bing, CHEN Jian, WANG Feng-gang, XIA Xing. Recovery of valuable metals from spent lithium-ion batteries by smelting reduction process based on $FeO-SiO_2-Al_2O_3$ slag system [J]. Transactions of Nonferrous Metals Society of China, 2017,

27: 450−456.

[6] HUANG Hong-jun, HUANG Qiu-sen. Mechanism of recycling electrode materials spent lithium batteries by ball milling-low temperature heat treatment-flotation [J]. The Chinese Journal of Nonferrous Metals, 2019, 29(4): 878−886. (in Chinese)

[7] LAI Yan-qing, YANG Jian, ZHANG Gang. Optimization and kinetics of leaching valuable metals from cathode materials of spent ternary lithium-ion batteries with starch as reducing agent [J]. The Chinese Journal of Nonferrous Metals, 2019, 29(1): 153−160. (in Chinese)

[8] ZHU Shu-guang, HE Wen-zhi, LI Guang-ming, ZHOU Xu, ZHANG Xiao-jun, HUANG Ju-wen. Recovery of Co and Li from spent lithium-ion batteries by combination method of acid leaching and chemical precipitation [J]. Transactions of Nonferrous Metals Society of China, 2012, 22: 2274−2281.

[9] GAO Jing, QIU Yun-ren, LI Mao-lin, LE Hui-shang. Separation of valuable metals in spent $LiNi_{0.46}Co_{0.2}Mn_{0.34}O_2$ battery by shear induced dissociation coupling with ultrafiltration [J]. Hydrometallurgy, 2019, 189: 105127.

[10] CHEN Xiang-ping, MA Hong-rui, LUO Chuan-bao, ZHOU Tao. Recovery of valuable metals from waste cathode materials of spent lithium-ion batteries using mild phosphoric acid [J]. Journal of Hazardous Materials, 2017, 326: 77−86.

[11] GUO Miao-miao, XI Xiao-li, ZHANG Yun-he. Recovering valuable metals from waste ternary cathode materials of power battery by combined high temperature hydrogen reduction and hydrometallurgy [J]. The Chinese Journal of Nonferrous Metals, 2020, 30(6): 1415−1426. (in Chinese)

[12] CAO Zhi-qin, ZHENG Xiao-hong, CAO Hong-bin, ZHAO He, SUN Zhi, GUO Zhuang, WANG Kai, ZHOU Bin. Efficient reuse of anode scrap from lithium-ion batteries as cathode for pollutant degradation in electro-Fenton process: Role of different recovery processes [J]. Chemical Engineering Journal, 2018, 337: 256−264.

[13] YAO Zhen, ZHONG Qi-fan, XIAO Jin, YE Sheng-chao, TANG Lei, ZHANG Zhen-hua. An environmental-friendly process for dissociating toxic substances and recovering valuable components from spent carbon cathode [J]. Journal of Hazardous Materials, 2021, 404: 124227.

[14] LIU Zhan-peng, GUO Yang, HE Wen-zhi, LI Guang-ming, ZHU Hao-chen. The leaching of lithium of anode active material in spent lithium ion battery [J]. Environmental Science & Technology, 2015, 38: 93−95, 99. (in Chinese)

[15] YU Xue-bin, FANG He-ping, GONG Wen-qi. Experimental study on upgrading of a fine-scaled graphite ore by flotation [J]. Journal of Wuhan University of Technology (Materials Science Edition), 2000, 15: 53−57.

[16] LI Hong-qiang, FENG Qi-ming, YANG Si-yuan, OU Le-ming, LU Ying. The entrainment behaviour of sericite in microcrystalline graphite flotation [J]. International Journal of Mineral Processing, 2014, 127: 1−9.

[17] ZAGHIB K, SONG X, GUERFI A, RIOUX R, KINOSHITA K. Purification process of natural graphite as anode for Li-ion batteries: chemical versus thermal [J]. Journal of Power Sources, 2003, 119: 8−15.

[18] LIU Feng-chun. Research on the method of alkali calcination on purification of graphite [J]. China Non-Metallic Minerals Industry, 2013, 4: 36−37, 41. (in Chinese)

[19] WANG Ying-wei, WU Peng, XU Chang-yao, YIN Shan. Purification of aphanitic graphite by alkali roasting under high temperature [J]. Carbon, 2008(1): 26−29. (in Chinese)

[20] LI Ji-ye, YAO Ming-de. Research on production of high-carbon graphite by chloridizing roast [J]. China Mining Magazine, 1996, 3: 45−48. (in Chinese)

[21] YANG Sen, YANG Shao-bin, DONG Wei, SHEN Ding. Purification process and reversible lithium storage performance of natural microcrystalline graphite [J]. Bulletin of the Chinese Ceramic Society, 2019, 38: 1148−1154. (in Chinese)

[22] YANG Wen-tao, YING Hang-jun, ZHANG Shun-long, GUO Rong-nan, WANG Jian-li, HAN Wei-qiang. Electrochemical performance enhancement of porous Si lithium-ion battery anode by integrating with optimized carbonaceous materials [J]. Electrochimica Acta, 2020, 337: 135687−135687.

[23] SRIDHAR D, MEUNIER J L, OMANOVIC S. Directly grown carbon nano-fibers on nickel foam as binder-free long-lasting supercapacitor electrodes [J]. Materials Chemistry and Physics, 2019, 223: 434−440.

[24] BIESINGER M C, PAYNE B P, GROSVENOR A P, LAU L W M, GERSON A R, SMART R S C. Resolving surface chemical states in XPS analysis of first row transition metals, oxides and hydroxides: Cr, Mn, Fe, Co and Ni [J]. Applied Surface Science, 2011, 257: 2717−2730.

[25] HAYASHI T, MAEYAMA S, YOSHII S. TEM, AES and XPS studies of Si layer on buried SiO_2 layer formed by high-dose oxygen ion-implantation [J]. Japanese Journal of Applied Physics, 2014, 19: 1111−1116.

[26] MORRISH R, WITVROUW A, MUSCAT A J. Kinetic to transport-limited anhydrous HF etching of silicon oxynitride films in supercritical CO_2 [J]. Journal of Physical Chemistry C, 2007, 111: 15251−15257.

[27] TSAI W C, WANG S K, HE T M, CHOU L C, HSIEH Y C, LIAO K Y, CHEN H C, WEN C R. Continuous-time photon-stimulated desorption spectroscopy studies on soft X-ray-induced reactions of CF_3Br adsorbed on Si(111)-7×7 [J]. Journal of Chemical Physics, 2011, 135: 2035.

[28] CHAI Zuo-qiang, WANG Zhi-xing, WANG Jie-xi, LI Xin-hai, GUO Hua-jun. Potentiostatic deposition of nickel cobalt sulfide nanosheet arrays as binder-free electrode for high-performance pseudocapacitor [J]. Ceramics International, 2018, 44: 15778−15784.

[29] WEI Wei, WU Ai-chun, QIAO Zhi-Wei, LI Shu-hua, LIANG Hong, PENG Feng. Effect of Sr and Fe doped $LaCoO_3$ on catalytic oxidation of soot and sulfur resistance [J]. Chinese Journal of Inorganic Chemistry, 2020, 36: 87−96. (in Chinese)

[30] MA Ling-ling, QIN Zhi-hong, ZHANG Lu, LIU Xu, CHEN Hang. Peak fitting methods and parameter settings in XPS analysis for organic sulfur in coal [J]. Journal of Fuel Chemistry and Technology, 2014, 42: 277−283. (in Chinese)

[31] YANG Li-jie, CHENG Xin-qun, MA Yu-lin, LOU Shuai-feng, CUI Ying-zhi, GUAN Ting, YIN Ge-ping. Changing of SEI film and electrochemical properties about MCMB electrodes during long-term charge/discharge cycles [J]. Journal of the Electrochemical Society, 2013, 160:

2093−2099.

[32] BEAMSON G, BRIGGS D. High resolution XPS of organic polymers: The Scienta ESCA300 database [J]. Journal of Chemical Education, 1992, 70: A25.

[33] HINA R, ARAFA I, ENNAB O. Hydrochlorination of $(CH_3)_3SiCHCl_2$ over Pd, Ni, Co and Fe supported on AlF_3 [J]. Journal of Chemical Sciences, 2017, 129: 353−358.

[34] ZHONG Jin-hui, WANG An-liang, LI Gao-ren, WANG Jian-wei, OU Yan-nan, TONG Ye-xiang. Co_3O_4/$Ni(OH)_2$ composite mesoporous nanosheet networks as a promising electrode for supercapacitor applications [J]. Journal of Materials Chemistry, 2012, 22: 5656−5665.

[35] LIU Kui, YANG Sheng-long, LAI Fei-yan, WANG Hong-qiang, HUANG Yon-guo, ZHENG Feng-hua, WANG Shu-bin, ZHANG Xiao-hui, LI Qing-yu. Innovative electrochemical strategy to recovery of cathode and efficient lithium leaching from spent lithium-ion batteries [J]. ACS Applied Energy Materials, 2020, 3: 4767−4776.

[36] YUE Peng, WANG Zhi-xing, LI Xin-hai, XIONG Xun-hui, WANG Jie-xi, WU Xian-wen, GUO Hua-jun. The enhanced electrochemical performance of $LiNi_{0.6}Co_{0.2}Mn_{0.2}O_2$ cathode materials by low temperature fluorine substitution [J]. Electrochimica Acta, 2013, 95: 112−118.

[37] LIN Jiao, LI Li, ERSHA F, LIU Chun-wei, ZHANG Xiao-dong, CAO Hong-bin, SUN Zhi, CHEN Ren-jie. Conversion mechanisms of selective extraction of lithium from spent lithium-ion batteries by sulfation roasting [J]. ACS Applied Materials & Interfaces, 2020, 12: 18482−18489.

[38] GUO De-chao, ZENG Xie-rong, DENG Fei, ZOU Ji-zhao, SHENG Hong-chao. Preparation and electrochemical performance of expanded graphites as anode materials for a lithium-ion battery [J]. New Carbon Materials, 2016, 98: 734−734. (in Chinese)

恒压酸浸法回收退役锂离子电池废炭渣

诸向东 [1]，肖 劲 [1,2]，毛秋云 [3]，张振华 [1]，唐 雷 [1]，仲奇凡 [1,2]

1. 中南大学 冶金与环境学院，长沙 410083；
2. 中南大学 难冶有色金属资源高效利用国家工程实验室，长沙 410083；
3. 湖南第一师范学院 教育科学学院，长沙 410205

摘 要：采用恒压酸浸技术，对废炭渣(WCR)进行高效解毒并再生成锂离子电池可用的高纯石墨产品(PGC)。运用正交试验和单因素试验相结合的方法，对浸出条件进行优化。结果表明，在浸出温度为 60 ℃、初始酸浓度为 12%、浸出时间为 180 min 和液固比为 25:1 的最优条件下，可获得符合商业石墨要求的 99.5%纯度石墨产品。同时，以氢氧化钠溶液为沉淀剂，在 pH=11 的条件下，镍、钴、锰和铝的回收率分别达到 96.92%、87.5%、97.83% 和 92.17%。此外，通过蒸发结晶工艺还可以回收纯度超过 99%的 NaF 副产物。整个流程中氟的损失率小于 0.5%，从而消除氟对环境的污染风险。此流程展现了可观的环境效益和经济效益。

关键词：恒压酸浸；废炭渣；阳极材料再生；氢氧化钠沉淀；氟化钠

(Edited by Bing YANG)